The Astrophysical Journal Letters, 889:L18 (9pp), 2020 January 20 https://doi.org/10.3847/2041-8213/ab665e

Coronal Properties of Black Hole X-Ray Binaries in the Hard State as Seen by *NuSTAR* and *Swift*

Zhen Yan[1], Fu-Guo Xie[1], and Wenda Zhang[2]
[1] Key Laboratory for Research in Galaxies and Cosmology, Shanghai Astronomical Observatory, Chinese Academy of Sciences, 80 Nandan Road, Shanghai 200030, People's Republic of China; zyan@shao.ac.cn, fgxie@shao.ac.cn
[2] Astronomical Institute, Czech Academy of Sciences, Boční II 1401, CZ-141 00 Prague, Czech Republic; zhang@asu.cas.cz
Received 2019 October 18; revised 2019 December 21; accepted 2019 December 27; published 2020 January 22

Abstract

In this work we measure two important phenomenological parameters of corona (and hot accretion flow) in black hole X-ray binaries: the photon index Γ and the electron temperature kT_e. Thanks to the capability of the *Nuclear Spectroscopic Telescope Array* in hard X-rays, we measure these two parameters over six orders of magnitude in the 0.1–100 keV X-ray luminosity L_x, from $\sim 5 \times 10^{38}$ erg s^{-1} down to as low as $\sim 5 \times 10^{32}$ erg s^{-1}. We confirm the existence of a "V"-shaped correlation between Γ and L_x. Surprisingly, we observe a "Λ"-shaped correlation between kT_e and L_x. The "cooler when brighter" branch in the high-luminosity regime ($L_x \gtrsim 3 \times 10^{36}$ erg s^{-1}) agrees with previous results and can be understood under the existing model of Compton scattering in the corona. On the other hand, the apparent "cooler when fainter" (positive kT_e–L_x correlation) branch in the low-luminosity regime ($L_x \lesssim 3 \times 10^{36}$ erg s^{-1}) is unexpected, thus it puts a new challenge to existing models of hot accretion flow/corona.

Unified Astronomy Thesaurus concepts: Accretion (14); Black hole physics (159); X-ray binary stars (1811); Black holes (162); Compact objects (288); High energy astrophysics (739); Compact binary stars (283)

1. Introduction

In the current understanding, the hard X-rays from active galactic nuclei (AGNs) and black hole X-ray binaries (BHXRBs) are produced by a central hot corona (or hot accretion flow; below we use them interchangeably). The soft seed photons, originating either externally from the underlying cold accretion disk or internally from the corona itself, are inversely Compton scattered by the hot electrons in the corona (see reviews by Done et al. 2007; Yuan & Narayan 2014). The corresponding hard X-ray continuum spectrum can be well described by a power-law shape, with a high-energy cutoff at tens to hundreds of keVs. The X-ray luminosity L_x, the photon index Γ, and the cutoff energy E_c determined from X-ray spectral fitting reveal important properties of the corona. For example, the cutoff energy empirically relates to the electron temperature kT_e as $E_c = 2 \sim 3\,kT_e$ (Petrucci et al. 2001), while the Γ is mostly determined by kT_e and optical depth (Titarchuk & Lyubarskij 1995; Zdziarski et al. 1996). With given kT_e and L_x, the optical depth then provides a constraint on the size of the corona.

Observationally the power-law index Γ can be measured much more easily than the electron temperature kT_e. The power-law index can be derived based on the X-ray spectrum below 10 keV, a band covered by most X-ray missions, among which some have high sensitivity. Consequently, the power-law indices have been extensively studied in BHXRBs and AGNs using different samples spanning a large range in X-ray luminosity (e.g., Younes et al. 2011; Yang et al. 2015). A "V" shape in the Γ–L_x diagram is found: below a certain luminosity ($\sim$1% L_{Edd}) the power-law index increases with a decreasing X-ray luminosity (so called "harder when brighter") and above that the power-law index increases with an increasing X-ray luminosity ("softer when brighter").

The hard and hard-intermediate states of BHXRBs, where the X-ray spectrum is usually dominated by the thermal Comptonization of the corona (Done et al. 2007; Yuan & Narayan 2014), provide an excellent opportunity to study the corona properties. In order to constrain the electron temperature kT_e (or cutoff energy E_c) of the corona, a high-quality X-ray spectrum extending to at least tens of keV are necessary. The most well-studied case is the prototype BHXRB GX 339-4 in its hard and hard-intermediate states, in which an anti-correlation between E_c and L_x has been found (e.g., Miyakawa et al. 2008; Motta et al. 2009). Similar anticorrelation in hard and/or hard-intermediate states has also been observed in other BHXRBs, such as XTE J1550−564 (Rodriguez et al. 2003) and GRO J1655−40 (Joinet et al. 2008).

Because of strong background, previous hard X-ray (above 10 keV) instruments are only capable of investigating bright sources, e.g., in most BHXRBs only the $L_x \gtrsim 10^{37}$ erg s^{-1} regime. Only close sources have good enough hard X-ray spectra to constrain the electron temperature (or cutoff energy). *Nuclear Spectroscopic Telescope Array* (*NuSTAR*; Harrison et al. 2013), the first focusing telescope in hard X-rays, has unprecedented sensitivity, low background, and no pile-up effect. It can provide high signal-to-noise ratio spectra at the 3–79 keV energy band for the corona at not only high but also low luminosities.

In this Letter, we combine the *NuSTAR* and *Swift* spectra to study the coronal properties (including Γ and kT_e) of the hard state of BHXRBs, with a focus on the low-luminosity regime, the electron temperature of which that was poorly explored before. Section 2 presents the sample selection and data analysis. Section 3 presents our results. Brief discussions and a summary are devoted to Section 4.

2. Sample Selection and Data Analysis

2.1. Sample/Data Selection

We list in Table 1 the sources selected in our sample and in Table 2 (in the Appendix) the details of each observation and

Table 1
Sample

Source	R.A.	Decl.	Distance (kpc)	References
Swift J1357.2−0933	13:57:16.84	−09:32:38.79	6.3	[1]
GS 1354−64	13:58:09.70	−64:44:05.80	25.0	[2]
MAXI J1535−571	15:35:19.73	−57:13:48.10	4.1	[3]
GX 339-4	17:02:49.31	−48:47:23.16	9.0	[4]
IGR J17091−3624	17:09:07.61	−36:24:25.70	12.0	[5]
GRS 1716−249	17:19:36.93	−25:01:03.43	2.4	[6]
GRS 1739−278	17:42:40.03	−27:44:52.70	7.5	[7]
H1743−322	17:46:15.60	−32:14:00.86	8.5	[8]
Swift J1753.5−0127	17:53:28.29	−01:27:06.26	7.15	[9]
MAXI J1813−095	18:13:34.07	−09:32:07.30		
MAXI J1820+070	18:20:21.90	+07:11:07.30	3.46	[9]
GRS 1915+105	19:15:11.55	+10:56:44.76	8.6	[10]
Cyg X-1	19:58:21.68	+35:12:05.78	1.86	[11]
V404 Cyg	20:24:03.82	+33:52:01.90	2.4	[12]

References. [1] Armas Padilla et al. (2014); [2] Corral-Santana et al. (2016); [3] Chauhan et al. (2019); [4] Heida et al. (2017); [5] Iyer et al. (2015); [6] della Valle et al. (1994); [7] Yan & Yu (2017); [8] Steiner et al. (2012); [9] Gandhi et al. (2019); [10] Reid et al. (2014); [11] Reid et al. (2011); [12] Miller-Jones et al. (2009).

spectral result (see Section 2.2 for details of the spectral modeling). We assume MAXI J1813−095 has a distance of 8 kpc, as it lacks a distance measurement (see Table 1).

Our motivation is to investigate the coronal properties; we thus first restrict to BHXRBs that have publicly available *NuSTAR* observations. *NuSTAR* lacks soft X-ray coverage below 3 keV, which is crucial for the thermal emission component. We then supplement during the spectral analysis with *Swift*/XRT observations that cover the 0.3–10 keV band. We cross-match the *NuSTAR* archive with the *Swift* archive for searching quasi-simultaneous observations within one day. The exact observational times of *NuSTAR* and *Swift* observations are given in Table 2 (in the Appendix).

We further select those whose X-ray spectra are dominated by the Comptonization emission. We thus take the following two criteria: one is that the X-ray spectrum can be well fitted with our model ($\chi^2 < 2$), and the other is that the X-ray flux from the Comptonization component contributes more than 70% of the total X-ray flux (see details in Section 2.2 and Figure 1). Observations that meet these two criteria are all in the hard or hard-intermediate states (Dunn et al. 2010). During this step, 4U 1630−472 and V4641 Sgr are excluded, since none of their observations meet these two criteria.

We notice that there are four *NuSTAR* observations that have no quasi-simultaneous (within one day) *Swift*/XRT observations. We still include them to enlarge our sample size at low luminosities. Among them, two have *Swift* observations within two days: the observation of V404 Cyg on modified Julian date (MJD) 56578 and the observation of GRS 1739−278 on MJD 57692. In this work, we still consider them as quasi-simultaneous observations. Meanwhile, the other two, MAXI J1820+070 on MJD 58604 and H1743−322 on MJD 57230, have no quasi-simultaneous *Swift* observations. They are also included in our sample, but during the spectral modeling, they are fit without the thermal *diskbb* component; see Section 2.2.

We additionally exclude from our sample the following *NuSTAR* observations based on various reasons. The observation of H1743−322 in its quiescent state on MJD 57250 is not included since it is not robustly detected. The observations of V404 Cyg on MJD 56198 and 57197 associate with many large amplitude flares, during which both the X-ray spectrum and the local absorption are highly variable (Walton et al. 2017).

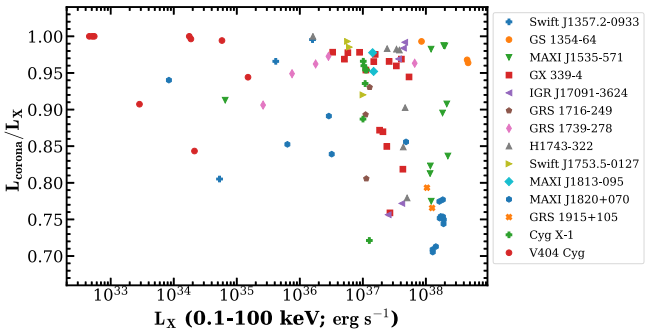

Figure 1. Corona radiation fraction L_{corona}/L_x for BHXRBs in their hard/hard-intermediate state. The uncertainties are not shown here for clarity.

Time-resolved spectra or flux-resolved spectra are necessary (e.g., Walton et al. 2017). We thus exclude these two observations to avoid the complexities mentioned above.

2.2. Data Reduction and Spectral Analysis

The *NuSTAR* data are processed through the NUPIPELINE task of the NUSTARDAS package contained in HEASoft 6.25, with calibration files of version 20181030. The source spectra were extracted using a circular region with a radius of 90″ at the source position, and the background spectra were extracted from an annulus with inner and outer radii of 180″ and 200″.

The *Swift*/XRT data were first processed with XRTPIPELINE (v 0.13.4) in order to generate the cleaned event file. We then extract the source and background spectra by using XSELECT, while the events at the central pixels were excluded if the data suffered from pile-up effects (Evans et al. 2009).

The joint spectral fitting of quasi-simultaneous *Swift*/XRT and *NuSTAR* observations was performed using PyXspec with XSPEC 12.10.1. For the modeling, we consider *Swift*/XRT and *NuSTAR* spectra in 0.5–10 keV and 4–78 keV, respectively.

We fit the spectra with a model that is an absorption of a combination of multi-colored disk blackbody (*diskbb*), thermal Comptonization (*nthcomp*; Zdziarski et al. 1996), and Gaussian iron line reflection (*Gauss*) components, i.e., *constant*tbabs* (diskbb+nthcomp+Gauss)* in XSPEC notation. Note that for the two cases without *Swift*/XRT observations, *diskbb* is omitted.

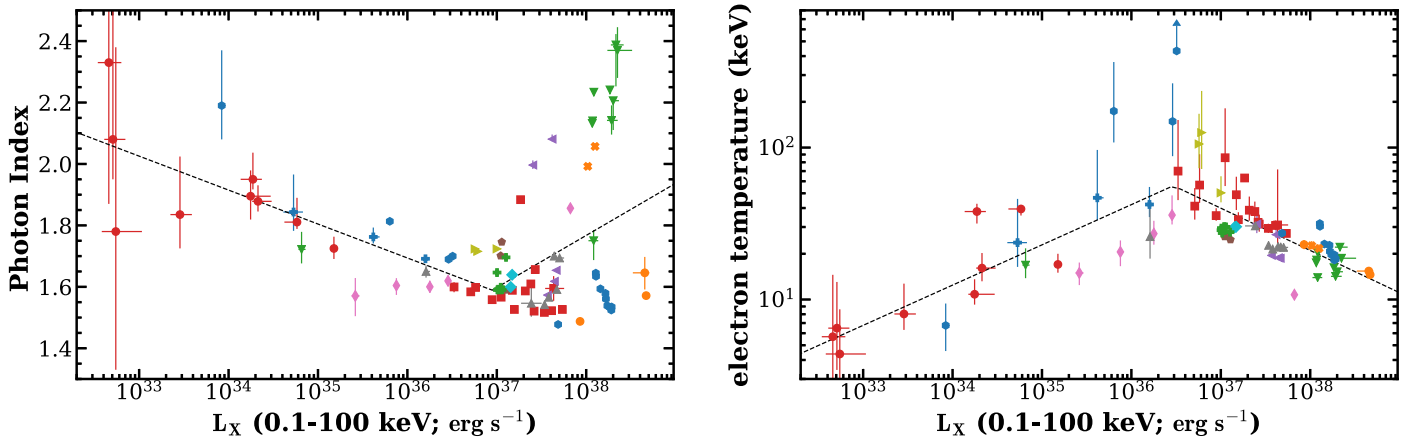

Figure 2. Relationship between photon index Γ and the X-ray luminosity L_x (left panel) and that between the electron temperature kT_e and the X-ray luminosity (right panel) for BHXRBs in their hard/hard-intermediate state. The figure legend is the same as in Figure 1.

Three observations (on MJD 56578, 56579, and 56628) of V404 Cyg are in the quiescent state; we only consider using the *nthcomp* component (see also Rana et al. 2016). For the absorption by the Galactic interstellar medium, the abundances and cross sections are set to Wilms et al. (2000) and Verner et al. (1996). Note that the column density N_H of Swift J1357.2−0933, MAXI J1820+070, and GRS 1915+105 is fixed to 0.012×10^{22} cm^{-2} (Beri et al. 2019), 0.15×10^{22} cm^{-2} (Uttley et al. 2018), and 6.5×10^{22} cm^{-2} (Miller et al. 2013), respectively, since they cannot be tightly and consistently constrained under our data set.

The thermal Comptonization model *nthcomp* includes three main parameters (Zdziarski et al. 1996): the power-law photon index Γ, the electron temperature kT_e, and the temperature of seed thermal photons kT_s. The kT_s is tied to the disk temperature when the *diskbb* component is applied. During the modeling, the value of *constant* is fixed for *NuSTAR*/FPMA, but is set free for *Swift*/XRT and *NuSTAR*/FPMB. Once the best-fitting result is derived, we then use the convolution model *cflux* to estimate the 0.1–100 keV X-ray fluxes for the three different components. In most cases parameters Γ and kT_e are well-constrained. Only for the observation of MAXI J1820+070 on MJD 58404, we have a lower limit constraint on kT_e.

3. Results

We first show in Figure 1 the fraction of corona luminosity, which is defined as the *nthcomp*-to-all luminosity ratio L_{corona}/L_x. Obviously because of the sample selection, all observations have $L_{corona}/L_x > 70\%$, i.e., all are dominated by corona emission.

The left panel of Figure 2 shows the correlation between the photon index Γ and the X-ray luminosity L_X. Obviously Γ and $\log(L_X)$ exhibit a "V"-shaped correlation, consistent with previous results (e.g., Yamaoka et al. 2005; Yuan et al. 2007; Wu & Gu 2008; Yang et al. 2015). We take the following piecewise linear function to fit the data:

$$Y(X) = \begin{cases} f_1(X - X_c) + Y_c & (X \leqslant X_c), \\ f_2(X - X_c) + Y_c & (X \geqslant X_c). \end{cases} \quad (1)$$

By replacing the X and Y with $\log L_x$ and Γ in Equation (1), we fit the Γ–L_x correlation by using the Levenberg–Marquardt method with the Python package LMFIT (Newville et al. 2014). The best-fit result is shown by the dashed curve in the left panel of Figure 2. We find the correlation slope turns between positive ($f_2 = 0.17 \pm 0.05$) and negative ($f_1 = -0.11 \pm 0.03$) at $\log L_x = 36.95 \pm 0.27$ ($L_x \sim 9 \times 10^{36}$ erg s^{-1}). For a 10 $M_\odot$ black hole, the turnover happens at nearly 0.01 L_{Edd}, which roughly agrees with previous results (e.g., Yuan et al. 2007; Wu & Gu 2008; Yang et al. 2015). The Spearman coefficients of the correlation for the data below and above this turning luminosity are −0.81 and 0.11 at the significances of 5.47σ and 0.81σ, respectively. Note that it seems that different sources/outbursts follow different tracks of the positive Γ–L_x correlation branch (see also in Yamaoka et al. 2005; Yang et al. 2015), which results in large scatters and low significance of the positive correlation.

We then investigate the relationship between the electron temperature kT_e and the X-ray luminosity L_x. As shown in the right panel of Figure 2, they follow a "Λ"-shaped kT_e–L_x correlation. Discarding the lower limit value of kT_e during the fitting, we find the turnover happens at $\log L_x = 36.47 \pm 0.15$ ($L_x \sim 3 \times 10^{36}$ erg s^{-1}), which is ∼1/3 that of the Γ–L_x correlation. Considering the uncertainties of the fitting results and large scatter of data, we caution that the exact difference in turnover luminosity awaits future investigations, either statistically or individually. The best-fit slopes of positive and negative branches are $f_1 = 0.26 \pm 0.03$ and $f_2 = -0.27 \pm 0.04$, respectively. The Spearman coefficients are 0.77 and −0.77 at the significances of 4.21σ and 8.06σ for the low- and high-luminosity branches, respectively. Admittedly, the chi-square of some observations at the high-luminosity branch are relatively larger with the thermal Comptonization model (see Table 2 in the Appendix). The estimation of kT_e is probably affected by the relativistic reflection components (see the discussion in Section 4.2). To avoid their contamination, we additionally exclude those data with reduced χ^2 greater than 1.3 and do the fitting again. The slope of the bright branch is now revised to $f_2 = -0.31 \pm 0.05$, which agrees with the previous value ($f_2 = -0.27 \pm 0.04$) within uncertainties. The Spearman coefficient of the remaining data is −0.81 at a significance of 7.97σ.

We emphasis that the "cooler when brighter" behavior above 3×10^{36} erg s^{-1} is consistent with previous results (e.g., Miyakawa et al. 2008; Motta et al. 2009). However, the "cooler when fainter" behavior with L_x spanning over ∼4 orders of

magnitude below 3×10^{36} erg s^{-1} has never been reported before.

Due to limitation in the sensitivity of the hard X-ray telescopes, previous studies of electron temperature kT_e mostly covered the $L_x > 10^{37}$ erg s^{-1} high-luminosity regime (e.g., Yamaoka et al. 2005; Joinet et al. 2008; Miyakawa et al. 2008; Motta et al. 2009), among which only a negative kT_e–L_x (in some cases, E_c–L_x) correlation is reported. For example, Yamaoka et al. (2005) have analyzed the X-ray spectra of nine BHXRBs with both *RXTE* and *Beppo-SAX* observations, and found a negative E_c–L_x correlation is observed for $L_x > 2 \times 10^{37}$ erg s^{-1}. However, as shown in their Figure 3, data of two nearby BHXRBs (XTE J118+480 and XTE J1650−500) below 2×10^{36} erg s^{-1} also hint at a positive relationship. Such turnover is ignored by Yamaoka et al. (2005), mostly because of the poor E_c measurement quality for L_x in the range 10^{36}–10^{37} erg s^{-1}.

For completeness, we also estimate the optical depth τ of the corona according to the following equation (Zdziarski et al. 1996):

$$\tau \approx \sqrt{\frac{9}{4} + \frac{m_e c^2}{kT_e} \frac{3}{(\Gamma - 1)(\Gamma + 2)}} - \frac{3}{2}, \quad (2)$$

i.e., τ can be crudely determined by kT_e and Γ. The results are listed in Table 2 (in the Appendix).

4. Summary and Discussions

Corona or hot accretion flow, which is responsible for the continuum emission in hard X-rays, is one of the key ingredients in black hole accretion systems. In this work, through a detailed modeling of quasi-simultaneous *NuSTAR* + *Swift* observations, we analyze the coronal properties of BHXRBs in their hard and hard-intermediate states that spans six orders of magnitudes of the luminosity range, from $\sim 5 \times 10^{32}$ to $\sim 5 \times 10^{38}$ erg s^{-1}.

We confirm previous work that Γ and L_x follow a "V"-shaped correlation, and the turnover happens at $L_x \approx 9 \times 10^{36}$erg s^{-1}. Meanwhile, we unexpectedly find a "Λ"-shaped relationship between electron temperature kT_e and L_x, i.e., it shows a "cooler when brighter" behavior when $L_x \gtrsim 3 \times 10^{36}$erg s^{-1}, and an opposite "cooler when fainter" behavior when $L_x \lesssim 3 \times 10^{36}$ erg s^{-1}. As discussed below, this result challenges the existing models of BHXRBs in the hard state.

4.1. Theoretical Implication

The leading model for the hard and hard-intermediate states of BHXRBs is the truncated accretion–jet model (Done et al. 2007; Yuan & Narayan 2014). In this model, the hard X-rays are produced by the inverse Compton scattering of electrons within the inner hot accretion flow, the residual thermal emission below ∼1–2 keV is mostly produced by the outer truncated cold Shakura–Sunyaev disk (SSD), and the radio up to infrared is from a relativistic jet.

This model has been applied to understand the "V"-shaped Γ–L_x correlation, where the primary reason for the opposite spectral behavior relates to the change in the origin/source of seed photons for the Compton scattering process (Yang et al. 2015). At the relative high accretion rate, the seed photons are mainly external, from quasi-thermal emission of cold clumps within the hot accretion flow (Yang et al. 2015) and/or SSD (Qiao & Liu 2013), while at a low accretion rate they are mainly internal, from synchrotron emission within the hot accretion flow/corona itself.

Despite the change in the seed photons, we should *always* expect that more radiative cooling (i.e., higher L_x) will result in cooler electrons, i.e., it should always follow a "cooler when brighter" track in the kT_e–L_x correlation, the case as observed for $L_x > 3 \times 10^{36}$ erg s^{-1}. $L_x < 3 \times 10^{36}$ erg s^{-1} represents the typical regime of the hot accretion flow, where theory predicts that the hot accretion flow will be closer to the ideal nonradiative or at least radiatively inefficient case (Yuan & Narayan 2014). In this regime, the electron temperature will reach its maximal value, nearly independent of accretion rate (or L_x). Obviously, such theoretical expectation contradicts the observation of the positive kT_e–L_x correlation branch, where the electrons become cooler at lower luminosity. Interestingly, we notice that Yu et al. (2015) investigated an optically thin but radiatively efficient accretion flow, where strong magnetic fields are considered to avoid thermal instabilities. In this model, a "cooler when fainter" behavior is indeed achieved (Yu et al. 2015). On the other hand, it has been noticed for a long time that quantitatively the observed electron temperature kT_e is systematically lower than that predicted by hot accretion flow (see, e.g., Yuan & Zdziarski 2004; Xie et al. 2010). Our measurements of kT_e are also much below the prediction of hot accretion flow, especially at the low-luminosity regime.

The other scenario in literature considers the possibility of electron–positron pair production (Svensson 1984; Coppi 1999). In this model, electron–positron pairs are created when energetic photons collide with one another. This process acts as an L_x/R-dependent thermostat (R is the size of emission site; see Svensson 1984; Coppi 1999), thus playing a major role in determining the outgoing spectrum and overall composition of the corona. This model predicts a negative $kT_e - L_x/R$ correlation (see e.g., Fabian et al. 2015). Obviously our results at low luminosities also contradict this model.

Another competing scenario suggested in the literature for the hard state of BHXRBs is the maximal jet model (e.g., Markoff et al. 2001, 2005).[3] In this model, the X-rays are the synchrotron emission of the accelerated particles in the jet base. However, synchrotron emission cannot produce a sharp cutoff feature in hard X-rays (Zdziarski et al. 2003). Moreover, it is still unclear to us how to understand in this model not only the newly discovered "Λ"-shaped kT_e–L_x relationship, but also the well-established "V"-shaped Γ–L_x correlation.

4.2. Reflection Emission

The reflection emission is known to have affects on the determination of kT_e (Fabian et al. 2015; García et al. 2015). However, the reflection emission in the low-luminosity regime ($L_x \lesssim 10^{37}$erg s^{-1}) is systematically weak (e.g., Fürst et al. 2016; Beri et al. 2019). For example, the reflection fraction is found to be less than 5% for a joint *NuSTAR* and *XMM-Newton* observation of GRS 1739−278 at $L_x \sim (2\text{–}3) \times 10^{35}$ erg s^{-1} (Fürst et al. 2016). Consequently, the cutoff energy and the kT_e constrained from the Comptonization model are consistent with those derived by reflection models (Fürst et al. 2016). Since we expect the reflection fraction to decrease with decreasing L_x, we thus argue that for $L_x \lesssim 3 \times 10^{36}$ erg s^{-1} the estimation of kT_e is insensitive to whichever reflection model is adopted. We

[3] Because of adopting an incorrect Bernoulli equation, the existence of the maximal jet model is challenged (Zdziarski 2016).

also emphasize that GRS 1739−278 individually also follows a positive kT_e–L_x correlation at the low-luminosity regime, as is clearly demonstrated in Figure 2.

We also examine our results by using the nonrelativistic reflection model *xillverCp*, which includes *nthcomp* as an incident spectrum. We find that (not shown here), although in numerous cases the exact value of kT_e is different from that derived by *nthcomp*, we still obtain a "Λ"-shaped kT_e–L_x correlation. The best-fit values of slopes of positive and negative branches are $f_1 = 0.11 \pm 0.02$ and $f_2 = -0.19 \pm 0.06$, respectively. The Spearman coefficients for the low- and high-luminosity branches are respectively 0.88 and −0.36 at the significances of 6.08σ and 2.10σ. The separation of the two branches locates at the luminosity $\log L_X = 36.94 \pm 0.24$. So our main conclusions are still solid with the reflection model. We do not report our results based on the *xillverCp* model, mainly because some bright observations are poorly fitted by this model (with reduced chi-square larger than two). The relativistic reflection model may be required for accurate estimation of kT_e in those bright observations. For example, Basak et al. (2017) also analyzed the *NuSTAR* data of the bright persistent BHXRB Cyg X-1. The kT_e derived by elaborated models (including multiple reflection components) is about 90 keV, which is roughly three times larger than our results (see also Ibragimov et al. 2005). On the other hand, this negative correlation at the high-luminosity branch has been demonstrated in previous studies with different models (e.g., Yamaoka et al. 2005; Fabian et al. 2015).

In this work we are not aimed at deriving the exact value of kT_e, but instead at the trend of the kT_e–L_x correlation, especially at the low-luminosity regime, which has been poorly investigated before. For this motivation, we adopt the same model for all the observations (see Section 2.2) instead of elaborately examining/modeling each observation in detail. The discrepancy of kT_e in different models is beyond the scope of this Letter.

4.3. Quiescent State of BHXRBs

All the data points with $L_x < 10^{33}$ erg s^{-1} are from V404 Cyg in its quiescent state (Plotkin et al. 2017). A component with a cutoff at ∼20 keV is clearly detected (Rana et al. 2016). However, the origin of the hard X-ray emission in the quiescent state remains unclear, and various models have been proposed (e.g., Narayan et al. 1996; Xie et al. 2014; Rana et al. 2016; Plotkin et al. 2017).

Although we cannot directly eliminate the debate, the data points in quiescent state roughly agree with the extrapolation (to the fainter end) of the two correlations observed in the low-luminosity regime of hard state, i.e., the negative Γ–L_x relationship (see the left panel of Figure 2 and also Plotkin et al. 2017) and the positive kT_e–L_x one (see the right panel of Figure 2). This implies that the hard X-rays in the quiescent state have the same origin as that in the faint-hard state, although the accretion physics in the latter is also unclear as of yet.

4.4. Corona in AGNs

A similar "V"-shaped Γ–L_x correlation has also been observed in AGNs (e.g., Younes et al. 2011; Yang et al. 2015), implying that the accretion physics in both stellar and supermassive black hole systems is at least similar (Yang et al. 2015).

The electron temperatures of the corona in AGNs have been probed extensively by various hard X-ray missions (e.g., Dadina 2007; Molina et al. 2013; Tortosa et al. 2018). A negative correlation between electron temperature (or cutoff energy) and the luminosity in the Eddington unit is reported by a sample of AGNs as observed by *Swift*/BAT (e.g., Ricci et al. 2018). However, this result is not confirmed by a smaller sample that is better in data quality (Molina et al. 2019; Rani et al. 2019). A large sample of AGNs (especially including the low-luminosity ones) is necessary to reach a consensus of coronal properties. If the accretion physics is similar, we will expect to observe a similar Λ-shaped correlation between kT_e and L_x in AGNs; or in other words, a different result will reveal distinctive differences between AGNs and BHXRBs.

We would like to thank Wenfei Yu and Anabella Araudo for discussion and Andrzej Zdziarski for his helpful comments. This research has made use of data and software provided by the High Energy Astrophysics Science Archive Research Center (HEASARC), which is a service of the Astrophysics Science Division at NASA/GSFC and the High Energy Astrophysics Division of the Smithsonian Astrophysical Observatory. Z.Y. and F.G.X. are supported in part by the National Program on Key Research and Development Project of China (grant 2016YFA0400704) and the Natural Science Foundation of China (grants 11773055, 11873074, U1938114, and U1838203). W.Z. acknowledges financial support provided by Czech Science Foundation grant 17-02430S. W.Z. is also supported by the project RVO:67985815.

Facilities: NuSTAR, *Swift*(XRT).

Appendix
Table of Observations and Spectral Fitting Result

In Table 2 we list all of the *NuSTAR* and/or *Swift* observations of each source and the best-fitting parameters of the coronae.

Table 2
List of Quasi-simultaneous Observations of *Swift* and *NuSTAR* and Best-fitting Parameters

Source	*NuSTAR*		*Swift*		Γ	kT_e (keV)	τ	Flux (0.1–100 keV) (erg s^{-1} cm^{-2})	χ^2/dof
	ObsID	Date(MJD)	ObsID	Date (MJD)					
Swift J1357.2-0933	90201057002	57871.54	00088094002	57871.62	$1.69^{+0.01}_{-0.01}$	$42.21^{+12.84}_{-7.33}$	$2.56^{+0.42}_{-0.42}$	$3.70^{+0.19}_{-0.07} \times 10^{-10}$	1160.47/1210
Swift J1357.2-0933	90301005002	57914.57	00031918066	57914.61	$1.76^{+0.03}_{-0.02}$	$46.70^{+49.76}_{-13.39}$	$2.20^{+1.05}_{-1.05}$	$9.65^{+1.70}_{-0.62} \times 10^{-11}$	385.48/422
Swift J1357.2-0933	90501325002	58632.51	00031918085	58632.29	$1.84^{+0.12}_{-0.06}$	$23.68^{+22.26}_{-7.29}$	$3.21^{+1.35}_{-1.35}$	$1.24^{+0.34}_{-0.29} \times 10^{-11}$	218.04/209
GS 1354-64	90101006002	57186.29	00033811005	57186.61	$1.49^{+0.01}_{-0.00}$	$23.00^{+1.56}_{-1.56}$	$4.94^{+0.21}_{-0.21}$	$1.14^{+0.03}_{-0.03} \times 10^{-9}$	1954.83/1839
GS 1354-64	90101006004	57214.57	00033811017	57214.35	$1.57^{+0.00}_{-0.00}$	$14.57^{+0.20}_{-0.26}$	$5.84^{+0.06}_{-0.06}$	$6.26^{+0.12}_{-0.17} \times 10^{-9}$	3301.82/2805
GS 1354-64	90101006006	57240.30	00033811040	57240.55	$1.65^{+0.05}_{-0.05}$	$15.39^{+0.54}_{-0.68}$	$5.18^{+0.33}_{-0.33}$	$6.04^{+0.75}_{-1.60} \times 10^{-9}$	3789.37/2852
MAXI J1535-571	90301013002	58003.78	00010264003	58004.28	$1.75^{+0.03}_{-0.06}$	$13.95^{+0.35}_{-0.49}$	$4.93^{+0.26}_{-0.26}$	$6.02^{+0.76}_{-0.75} \times 10^{-8}$	6878.04/3923
MAXI J1535-571	80302309002	58008.54	00010264005	58008.26	$2.24^{+0.01}_{-0.01}$	$16.21^{+0.75}_{-0.68}$	$3.00^{+0.09}_{-0.09}$	$9.16^{+0.20}_{-0.16} \times 10^{-8}$	3117.38/2613
MAXI J1535-571	80402302002	58010.22	00010264006	58010.93	$2.14^{+0.05}_{-0.05}$	$14.21^{+0.49}_{-0.32}$	$3.51^{+0.14}_{-0.14}$	$9.55^{+1.63}_{-1.06} \times 10^{-8}$	3133.83/2795
MAXI J1535-571	80402302004	58010.55	00010264006	58010.93	$2.21^{+0.01}_{-0.10}$	$15.23^{+0.55}_{-0.24}$	$3.20^{+0.13}_{-0.13}$	$9.96^{+1.59}_{-0.52} \times 10^{-8}$	3235.94/2821
MAXI J1535-571	80302309004	58013.17	00088245001	58013.18	$2.39^{+0.04}_{-0.13}$	$22.11^{+0.72}_{-0.78}$	$2.19^{+0.14}_{-0.14}$	$1.07^{+0.23}_{-0.13} \times 10^{-7}$	3795.49/2522
MAXI J1535-571	80302309006	58013.44	00088245001	58013.18	$2.37^{+0.08}_{-0.09}$	$18.69^{+0.77}_{-0.57}$	$2.49^{+0.15}_{-0.15}$	$1.11^{+0.51}_{-0.25} \times 10^{-7}$	4733.99/2830
MAXI J1535-571	80302309014	58048.88	00088245004	58048.99	$2.23^{+0.01}_{-0.01}$	$20.33^{+1.00}_{-0.81}$	$2.59^{+0.08}_{-0.08}$	$6.05^{+0.13}_{-0.12} \times 10^{-8}$	3414.27/2786
MAXI J1535-571	80402302009	58050.96	00088246001	58050.98	$2.14^{+0.01}_{-0.01}$	$18.19^{+1.20}_{-0.73}$	$2.98^{+0.11}_{-0.11}$	$5.86^{+0.16}_{-0.14} \times 10^{-8}$	2582.16/2478
MAXI J1535-571	80402302010	58051.36	00088246001	58050.98	$2.13^{+0.01}_{-0.01}$	$17.47^{+0.84}_{-0.61}$	$3.08^{+0.09}_{-0.09}$	$5.81^{+0.16}_{-0.13} \times 10^{-8}$	2978.61/2781
MAXI J1535-571	90501314002	58587.55	00088862002	58587.54	$1.72^{+0.06}_{-0.05}$	$16.84^{+4.88}_{-3.02}$	$4.51^{+0.70}_{-0.70}$	$3.26^{+0.35}_{-0.25} \times 10^{-11}$	656.60/789
GX 339-4	80001013002	56515.99	00032490015	56516.02	$1.53^{+0.00}_{-0.00}$	$33.55^{+3.98}_{-3.01}$	$3.68^{+0.25}_{-0.25}$	$1.62^{+0.02}_{-0.02} \times 10^{-9}$	2086.36/2213
GX 339-4	80001013004	56520.71	00080180001	56520.77	$1.52^{+0.00}_{-0.00}$	$32.14^{+4.20}_{-3.06}$	$3.82^{+0.28}_{-0.28}$	$2.70^{+0.05}_{-0.05} \times 10^{-9}$	2484.27/2453
GX 339-4	80001013006	56528.53	00080180002	56528.17	$1.52^{+0.00}_{-0.00}$	$30.73^{+2.36}_{-2.06}$	$3.92^{+0.18}_{-0.18}$	$4.22^{+0.05}_{-0.05} \times 10^{-9}$	2793.80/2706
GX 339-4	80001013007	56538.38	00032898013	56537.79	$1.59^{+0.04}_{-0.04}$	$30.95^{+40.85}_{-7.75}$	$3.54^{+1.81}_{-1.81}$	$4.46^{+1.38}_{-0.87} \times 10^{-9}$	577.60/563
GX 339-4	80001013008	56538.41	00032898013	56537.79	$1.53^{+0.00}_{-0.00}$	$27.22^{+0.87}_{-0.97}$	$4.21^{+0.09}_{-0.09}$	$5.58^{+0.08}_{-0.07} \times 10^{-9}$	3632.28/3414
GX 339-4	80001013010	56581.99	00032898035	56581.56	$1.56^{+0.00}_{-0.00}$	$35.67^{+4.22}_{-2.69}$	$3.39^{+0.21}_{-0.21}$	$9.16^{+0.14}_{-0.10} \times 10^{-10}$	2458.88/2473
GX 339-4	80102011002	57262.55	00032898124	57263.37	$1.66^{+0.01}_{-0.01}$	$31.38^{+4.79}_{-3.43}$	$3.25^{+0.28}_{-0.28}$	$2.78^{+0.08}_{-0.08} \times 10^{-9}$	2289.81/2219
GX 339-4	80102011003	57267.49	00032898126	57268.03	$1.88^{+0.00}_{-0.00}$	$63.06^{+0.00}_{-0.01}$	$1.55^{+0.00}_{-0.00}$	$1.90^{+0.00}_{-0.00} \times 10^{-9}$	509.07/536
GX 339-4	80102011004	57267.53	00032898126	57268.03	$1.61^{+0.00}_{-0.01}$	$37.94^{+6.16}_{-4.73}$	$3.04^{+0.29}_{-0.29}$	$2.48^{+0.09}_{-0.08} \times 10^{-9}$	2268.84/2220
GX 339-4	80102011006	57272.62	00032898130	57272.02	$1.59^{+0.01}_{-0.01}$	$38.70^{+8.90}_{-5.64}$	$3.09^{+0.39}_{-0.39}$	$2.15^{+0.08}_{-0.06} \times 10^{-9}$	2137.45/2144
GX 339-4	80102011008	57277.66	00081534001	57277.68	$1.59^{+0.01}_{-0.01}$	$48.93^{+15.36}_{-10.10}$	$2.63^{+0.47}_{-0.47}$	$1.54^{+0.03}_{-0.03} \times 10^{-9}$	1821.91/1760
GX 339-4	80102011010	57282.42	00032898138	57282.00	$1.57^{+0.01}_{-0.01}$	$85.72^{+95.55}_{-29.90}$	$1.83^{+0.97}_{-0.97}$	$1.15^{+0.03}_{-0.03} \times 10^{-9}$	1992.58/2004
GX 339-4	80102011012	57295.05	00081534005	57295.23	$1.60^{+0.01}_{-0.01}$	$56.66^{+33.73}_{-13.38}$	$2.35^{+0.68}_{-0.68}$	$5.97^{+0.16}_{-0.12} \times 10^{-10}$	1539.28/1547
GX 339-4	80302304002	58028.15	00032898148	58027.28	$1.60^{+0.02}_{-0.02}$	$70.01^{+81.88}_{-24.91}$	$2.02^{+1.10}_{-1.10}$	$3.43^{+0.12}_{-0.10} \times 10^{-10}$	1029.14/982
GX 339-4	80302304004	58051.57	00032898158	58051.38	$1.52^{+0.00}_{-0.01}$	$29.39^{+2.14}_{-1.96}$	$4.06^{+0.18}_{-0.18}$	$3.51^{+0.09}_{-0.06} \times 10^{-9}$	2379.42/2302
GX 339-4	80302304007	58148.36	00032898163	58148.16	$1.58^{+0.01}_{-0.01}$	$41.17^{+12.90}_{-7.61}$	$2.98^{+0.50}_{-0.50}$	$5.28^{+0.13}_{-0.15} \times 10^{-10}$	1311.36/1337
IGR J17091-3624	80001041002	57454.08	00031921099	57454.08	$1.57^{+0.00}_{-0.00}$	$19.52^{+0.95}_{-0.54}$	$4.87^{+0.12}_{-0.12}$	$2.14^{+0.07}_{-0.03} \times 10^{-9}$	2760.57/2665
IGR J17091-3624	80202014002	57459.59	00031921104	57459.58	$1.62^{+0.01}_{-0.00}$	$18.83^{+0.82}_{-0.71}$	$4.72^{+0.12}_{-0.12}$	$2.56^{+0.04}_{-0.04} \times 10^{-9}$	2386.88/2381
IGR J17091-3624	80202014004	57461.81	00031921106	57461.90	$1.65^{+0.00}_{-0.00}$	$18.67^{+0.66}_{-0.64}$	$4.55^{+0.10}_{-0.10}$	$2.68^{+0.04}_{-0.04} \times 10^{-9}$	2332.66/2283
IGR J17091-3624	80202014006	57476.11	00031921118	57475.59	$2.08^{+0.02}_{-0.01}$	$26.72^{+3.86}_{-1.35}$	$2.41^{+0.16}_{-0.16}$	$2.41^{+0.09}_{-0.09} \times 10^{-9}$	2354.90/2183
IGR J17091-3624	80202015004	57534.66	00081917002	57534.67	$2.00^{+0.02}_{-0.01}$	$31.41^{+4.91}_{-4.07}$	$2.31^{+0.23}_{-0.23}$	$1.47^{+0.07}_{-0.06} \times 10^{-9}$	1951.30/1943
GRS 1716-249	80201034007	57781.31	00034924001	57781.00	$1.59^{+0.00}_{-0.00}$	$24.77^{+0.51}_{-0.44}$	$4.11^{+0.05}_{-0.05}$	$1.86^{+0.03}_{-0.01} \times 10^{-8}$	4428.11/4079
GRS 1716-249	90202055002	57850.60	00034924029	57850.37	$1.70^{+0.00}_{-0.00}$	$25.95^{+1.21}_{-0.84}$	$3.50^{+0.09}_{-0.09}$	$1.60^{+0.02}_{-0.02} \times 10^{-8}$	4352.30/3511

Table 2
(Continued)

Source	*NuSTAR*		*Swift*		Γ	kT_e (keV)	τ	Flux (0.1–100 keV) (erg s^{-1} cm^{-2})	χ^2/dof
	ObsID	Date(MJD)	ObsID	Date (MJD)					
GRS 1716-249	90202055004	57853.69	00034924031	57853.88	$1.75^{+0.00}_{-0.00}$	$26.78^{+1.27}_{-1.36}$	$3.27^{+0.11}_{-0.11}$	$1.65^{+0.02}_{-0.02} \times 10^{-8}$	3588.63/3340
GRS 1739-278	80002018002	56742.67	00033203003	56742.15	$1.86^{+0.01}_{-0.00}$	$10.75^{+0.12}_{-0.10}$	$5.24^{+0.04}_{-0.04}$	$9.89^{+0.12}_{-0.11} \times 10^{-9}$	4436.78/3162
GRS 1739-278	80101050002	57280.88	00081764002	57280.93	$1.57^{+0.06}_{-0.07}$	$14.95^{+2.56}_{-2.51}$	$5.75^{+0.73}_{-0.73}$	$3.89^{+0.44}_{-0.36} \times 10^{-11}$	767.09/793
GRS 1739-278	80102101002	57660.89	00033812058	57661.07	$1.62^{+0.02}_{-0.01}$	$35.95^{+12.50}_{-4.77}$	$3.11^{+0.50}_{-0.50}$	$4.23^{+0.16}_{-0.11} \times 10^{-10}$	1268.15/1339
GRS 1739-278	80102101004	57680.63	00081979001	57680.76	$1.60^{+0.02}_{-0.03}$	$20.57^{+3.90}_{-4.00}$	$4.54^{+0.56}_{-0.56}$	$1.12^{+0.07}_{-0.07} \times 10^{-10}$	847.17/1002
GRS 1739-278	80102101005	57692.84	00033812067	57691.10	$1.60^{+0.02}_{-0.02}$	$27.13^{+5.83}_{-4.17}$	$3.83^{+0.46}_{-0.46}$	$2.65^{+0.11}_{-0.10} \times 10^{-10}$	1033.37/1026
H1743-322	80001044002	56918.65	00031121055	56918.35	$1.54^{+0.00}_{-0.00}$	$22.70^{+0.84}_{-0.61}$	$4.62^{+0.09}_{-0.09}$	$3.96^{+0.05}_{-0.03} \times 10^{-9}$	3246.68/3143
H1743-322	80001044004	56923.76	00031121061	56924.08	$1.59^{+0.00}_{-0.01}$	$22.08^{+0.60}_{-0.64}$	$4.41^{+0.08}_{-0.08}$	$5.43^{+0.15}_{-0.12} \times 10^{-9}$	3341.25/3185
H1743-322	80001044006	56939.76	00080797002	56940.20	$1.57^{+0.00}_{-0.00}$	$21.45^{+0.66}_{-0.86}$	$4.64^{+0.10}_{-0.10}$	$4.40^{+0.05}_{-0.06} \times 10^{-9}$	2901.29/2924
H1743-322	80002040002	57206.12	00080797003	57206.31	$1.55^{+0.07}_{-0.04}$	$30.50^{+1.18}_{-1.71}$	$3.81^{+0.31}_{-0.31}$	$2.81^{+0.86}_{-0.65} \times 10^{-9}$	2338.93/2357
H1743-322	80002040004	57230.16	…	…	$1.65^{+0.02}_{-0.02}$	$25.92^{+18.68}_{-7.34}$	$3.71^{+1.20}_{-1.20}$	$1.87^{+0.20}_{-0.10} \times 10^{-10}$	931.74/959
H1743-322	80202012002	57460.07	00031441056	57460.24	$1.69^{+0.00}_{-0.00}$	$22.02^{+0.79}_{-0.59}$	$3.92^{+0.08}_{-0.08}$	$5.83^{+0.71}_{-0.61} \times 10^{-9}$	3504.28/3303
H1743-322	80202012004	57462.28	00031441058	57462.90	$1.70^{+0.00}_{-0.00}$	$22.33^{+0.74}_{-0.47}$	$3.86^{+0.07}_{-0.07}$	$5.07^{+0.40}_{-0.34} \times 10^{-9}$	3495.04/3386
Swift J1753.5-0127	80002021002	56751.15	00080730001	56752.02	$1.72^{+0.00}_{-0.00}$	$105.54^{+61.31}_{-32.43}$	$1.26^{+0.43}_{-0.43}$	$9.33^{+0.17}_{-0.05} \times 10^{-10}$	1903.75/1917
Swift J1753.5-0127	80002021003	56751.89	00080730001	56752.02	$1.72^{+0.00}_{-0.01}$	$125.46^{+110.42}_{-53.18}$	$1.12^{+0.57}_{-0.57}$	$9.98^{+0.20}_{-0.18} \times 10^{-10}$	1908.30/1911
Swift J1753.5-0127	30001148002	56913.41	00080770001	56913.49	$1.72^{+0.00}_{-0.00}$	$50.34^{+14.40}_{-6.74}$	$2.18^{+0.32}_{-0.32}$	$1.64^{+0.04}_{-0.04} \times 10^{-9}$	2400.69/2316
MAXI J1813-095	80402303004	58183.60	00088654002	58183.56	$1.60^{+0.01}_{-0.01}$	$29.94^{+3.26}_{-2.49}$	$3.60^{+0.22}_{-0.22}$	$1.87^{+0.03}_{-0.03} \times 10^{-9}$	2084.45/2127
MAXI J1813-095	80402303006	58202.73	00088654004	58202.84	$1.64^{+0.01}_{-0.01}$	$30.15^{+3.41}_{-2.45}$	$3.41^{+0.22}_{-0.22}$	$1.94^{+0.07}_{-0.05} \times 10^{-9}$	2199.20/2162
MAXI J1820+070	90401309002	58191.85	00010627001	58191.87	$1.48^{+0.00}_{-0.00}$	$27.32^{+0.59}_{-0.61}$	$4.50^{+0.06}_{-0.06}$	$3.38^{+0.05}_{-0.05} \times 10^{-8}$	4746.61/3842
MAXI J1820+070	90401309004	58198.02	00010627009	58197.77	$1.53^{+0.00}_{-0.00}$	$19.65^{+0.53}_{-0.22}$	$5.11^{+0.06}_{-0.06}$	$1.30^{+0.02}_{-0.01} \times 10^{-7}$	4493.20/3602
MAXI J1820+070	90401309006	58198.30	00010627010	58198.78	$1.52^{+0.00}_{-0.00}$	$18.54^{+0.25}_{-0.25}$	$5.35^{+0.05}_{-0.05}$	$1.33^{+0.01}_{-0.01} \times 10^{-7}$	5195.07/3865
MAXI J1820+070	90401309008	58201.52	00010627013	58201.11	$1.53^{+0.00}_{-0.00}$	$18.22^{+0.31}_{-0.22}$	$5.35^{+0.05}_{-0.05}$	$1.30^{+0.01}_{-0.01} \times 10^{-7}$	4338.68/3608
MAXI J1820+070	90401309010	58201.85	00010627014	58202.17	$1.53^{+0.00}_{-0.00}$	$18.43^{+0.41}_{-0.28}$	$5.30^{+0.06}_{-0.06}$	$1.34^{+0.02}_{-0.02} \times 10^{-7}$	4476.90/3561
MAXI J1820+070	90401309012	58212.19	00088657001	58212.20	$1.54^{+0.00}_{-0.00}$	$19.78^{+0.18}_{-0.18}$	$5.05^{+0.03}_{-0.03}$	$1.20^{+0.01}_{-0.01} \times 10^{-7}$	6307.59/4206
MAXI J1820+070	90401309013	58224.93	00010627043	58224.95	$1.58^{+0.00}_{-0.00}$	$22.75^{+0.66}_{-0.80}$	$4.40^{+0.09}_{-0.09}$	$1.15^{+0.02}_{-0.01} \times 10^{-7}$	3871.94/3242
MAXI J1820+070	90401309014	58225.27	00010627045	58225.47	$1.56^{+0.00}_{-0.00}$	$20.75^{+0.23}_{-0.23}$	$4.76^{+0.03}_{-0.03}$	$1.16^{+0.01}_{-0.01} \times 10^{-7}$	6038.07/4112
MAXI J1820+070	90401309016	58241.79	00088657003	58241.67	$1.59^{+0.00}_{-0.00}$	$23.18^{+0.38}_{-0.29}$	$4.27^{+0.04}_{-0.04}$	$1.01^{+0.01}_{-0.01} \times 10^{-7}$	6766.12/4165
MAXI J1820+070	90401309018	58255.15	00088657004	58255.90	$1.64^{+0.00}_{-0.00}$	$31.61^{+1.58}_{-1.67}$	$3.28^{+0.11}_{-0.11}$	$8.94^{+0.09}_{-0.10} \times 10^{-8}$	4277.60/3270
MAXI J1820+070	90401309019	58255.60	00088657004	58255.90	$1.63^{+0.00}_{-0.00}$	$30.32^{+1.02}_{-1.01}$	$3.42^{+0.07}_{-0.07}$	$8.98^{+0.04}_{-0.09} \times 10^{-8}$	6821.45/3946
MAXI J1820+070	90401309037	58404.95	00010627112	58404.26	$1.70^{+0.01}_{-0.00}$	$1000.00^{+0.00}_{-567.61}$	$0.19^{+0.05}_{-0.05}$	$2.24^{+0.09}_{-0.08} \times 10^{-9}$	1975.57/1939
MAXI J1820+070	90401309039	58420.05	00010627120	58419.60	$1.81^{+0.00}_{-0.01}$	$173.74^{+191.84}_{-65.69}$	$0.76^{+0.47}_{-0.47}$	$4.44^{+0.17}_{-0.14} \times 10^{-10}$	2116.84/2065
MAXI J1820+070	90501311002	58567.83	00010627149	58567.16	$1.69^{+0.00}_{-0.00}$	$148.69^{+116.01}_{-60.93}$	$1.01^{+0.48}_{-0.48}$	$2.02^{+0.08}_{-0.06} \times 10^{-9}$	2283.13/2296
MAXI J1820+070	90501320002	58604.40	…	…	$2.19^{+0.18}_{-0.11}$	$6.75^{+2.66}_{-2.17}$	$5.41^{+1.29}_{-1.29}$	$5.85^{+0.64}_{-0.41} \times 10^{-12}$	871.47/998
GRS 1915+105	90201053002	57840.67	00080228002	57840.82	$2.06^{+0.01}_{-0.01}$	$21.68^{+1.40}_{-1.20}$	$2.83^{+0.12}_{-0.12}$	$1.42^{+0.03}_{-0.03} \times 10^{-8}$	3326.08/2846
GRS 1915+105	90301001002	57875.18	00088091001	57875.48	$1.99^{+0.01}_{-0.01}$	$22.62^{+1.63}_{-1.23}$	$2.90^{+0.13}_{-0.13}$	$1.18^{+0.03}_{-0.04} \times 10^{-8}$	3166.05/2830
Cyg X-1	30001011005	56776.92	00080732001	56776.89	$1.70^{+0.00}_{-0.00}$	$27.75^{+1.07}_{-1.07}$	$3.37^{+0.09}_{-0.09}$	$3.06^{+0.04}_{-0.04} \times 10^{-8}$	4258.02/3626
Cyg X-1	30001011007	56797.24	00080732002	56798.01	$1.65^{+0.00}_{-0.00}$	$28.59^{+0.78}_{-0.60}$	$3.50^{+0.06}_{-0.06}$	$2.43^{+0.02}_{-0.02} \times 10^{-8}$	5048.51/4163
Cyg X-1	90101020002	57429.45	00081820001	57429.55	$1.60^{+0.00}_{-0.00}$	$30.04^{+1.35}_{-0.91}$	$3.59^{+0.09}_{-0.09}$	$2.67^{+0.02}_{-0.02} \times 10^{-8}$	4346.34/3871

Table 2
(Continued)

Source	*NuSTAR*		*Swift*		Γ	kT_e (keV)	τ	Flux (0.1–100 keV) (erg s^{-1} cm^{-2})	χ^2/dof
	ObsID	Date(MJD)	ObsID	Date (MJD)					
Cyg X-1	30002150004	57537.89	00034310002	57537.54	$1.59^{+0.00}_{-0.00}$	$30.06^{+0.53}_{-0.66}$	$3.63^{+0.05}_{-0.05}$	$2.76^{+0.01}_{-0.01} \times 10^{-8}$	6582.65/4512
Cyg X-1	30002150006	57539.91	00034310003	57539.55	$1.59^{+0.00}_{-0.00}$	$30.16^{+0.51}_{-0.64}$	$3.62^{+0.04}_{-0.04}$	$2.63^{+0.01}_{-0.01} \times 10^{-8}$	6364.94/4494
Cyg X-1	30002150008	57541.92	00034310004	57541.48	$1.59^{+0.00}_{-0.00}$	$29.51^{+0.75}_{-0.68}$	$3.68^{+0.06}_{-0.06}$	$2.45^{+0.01}_{-0.01} \times 10^{-8}$	5207.24/4264
Cyg X-1	30202032002	57587.65	00081903001	57587.72	$1.59^{+0.00}_{-0.00}$	$27.39^{+0.97}_{-0.84}$	$3.84^{+0.08}_{-0.08}$	$2.51^{+0.02}_{-0.02} \times 10^{-8}$	4016.08/3798
V404 Cyg	30001010002	56578.50	00080264001	56579.78	$2.33^{+1.01}_{-0.46}$	$5.69^{+8.85}_{-3.30}$	$5.50^{+4.31}_{-4.31}$	$6.64^{+2.53}_{-1.64} \times 10^{-13}$	127.48/154
V404 Cyg	30001010003	56579.91	00080264001	56579.78	$2.08^{+0.42}_{-0.13}$	$6.48^{+6.57}_{-3.04}$	$5.98^{+2.90}_{-2.90}$	$7.38^{+2.80}_{-1.47} \times 10^{-13}$	203.23/209
V404 Cyg	30001010005	56628.73	00080264002	56628.75	$1.78^{+0.60}_{-0.45}$	$4.38^{+4.24}_{-3.05}$	$9.50^{+6.27}_{-6.27}$	$7.95^{+7.63}_{-2.41} \times 10^{-13}$	79.74/79
V404 Cyg	90102007005	57204.05	00031403068	57203.93	$1.72^{+0.04}_{-0.03}$	$17.02^{+2.98}_{-2.00}$	$4.47^{+0.44}_{-0.44}$	$2.19^{+0.17}_{-0.14} \times 10^{-10}$	1148.85/1217
V404 Cyg	90102007007	57209.28	00031403080	57209.51	$1.90^{+0.08}_{-0.08}$	$10.83^{+2.76}_{-1.57}$	$5.05^{+0.71}_{-0.71}$	$2.56^{+1.74}_{-0.38} \times 10^{-11}$	363.57/449
V404 Cyg	90102007009	57211.97	00031403085	57211.72	$1.88^{+0.05}_{-0.03}$	$16.10^{+4.13}_{-2.92}$	$4.00^{+0.58}_{-0.58}$	$3.10^{+1.30}_{-0.43} \times 10^{-11}$	830.18/857
V404 Cyg	90102007011	57226.35	00031403109	57226.40	$1.84^{+0.19}_{-0.11}$	$8.03^{+4.69}_{-1.72}$	$6.36^{+1.72}_{-1.72}$	$4.15^{+1.49}_{-0.91} \times 10^{-12}$	220.02/249
V404 Cyg	90102007013	57380.43	00031403122	57380.62	$1.81^{+0.08}_{-0.02}$	$39.44^{+2.31}_{-3.73}$	$2.35^{+0.18}_{-0.18}$	$8.45^{+0.67}_{-2.34} \times 10^{-11}$	935.86/900
V404 Cyg	90102007015	57393.64	00031403145	57393.57	$1.95^{+0.09}_{-0.03}$	$37.93^{+4.74}_{-6.30}$	$2.11^{+0.25}_{-0.25}$	$2.72^{+0.71}_{-0.73} \times 10^{-11}$	690.02/751

ORCID iDs

Zhen Yan https://orcid.org/0000-0002-5385-9586
Fu-Guo Xie https://orcid.org/0000-0001-9969-2091
Wenda Zhang https://orcid.org/0000-0003-1702-4917

References

Armas Padilla, M., Wijnands, R., Degenaar, N., et al. 2014, MNRAS, 444, 902
Basak, R., Zdziarski, A. A., Parker, M., & Islam, N. 2017, MNRAS, 472, 4220
Beri, A., Tetarenko, B. E., Bahramian, A., et al. 2019, MNRAS, 485, 3064
Chauhan, J., Miller-Jones, J. C. A., Anderson, G. E., et al. 2019, MNRAS Letters, 488, L129
Coppi, P. S. 1999, in ASP Conf. Ser. 161, High Energy Processes in Accreting Black Holes, ed. J. Poutanen & R. Svensson (San Francisco, CA: ASP), 375
Corral-Santana, J. M., Casares, J., Muñoz-Darias, T., et al. 2016, A&A, 587, A61
Dadina, M. 2007, A&A, 461, 1209
della Valle, M., Mirabel, I. F., & Rodriguez, L. F. 1994, A&A, 290, 803
Done, C., Gierliński, M., & Kubota, A. 2007, A&ARv, 15, 1
Dunn, R. J. H., Fender, R. P., Körding, E. G., Belloni, T., & Cabanac, C. 2010, MNRAS, 403, 61
Evans, P. A., Beardmore, A. P., Page, K. L., et al. 2009, MNRAS, 397, 1177
Fabian, A. C., Lohfink, A., Kara, E., et al. 2015, MNRAS, 451, 4375
Fürst, F., Tomsick, J. A., Yamaoka, K., et al. 2016, ApJ, 832, 115
Gandhi, P., Rao, A., Johnson, M. A. C., Paice, J. A., & Maccarone, T. J. 2019, MNRAS, 485, 2642
García, J. A., Steiner, J. F., McClintock, J. E., et al. 2015, ApJ, 813, 84
Harrison, F. A., Craig, W. W., Christensen, F. E., et al. 2013, ApJ, 770, 103
Heida, M., Jonker, P. G., Torres, M. A. P., & Chiavassa, A. 2017, ApJ, 846, 132
Ibragimov, A., Poutanen, J., Gilfanov, M., Zdziarski, A. A., & Shrader, C. R. 2005, MNRAS, 362, 1435
Iyer, N., Nandi, A., & Mandal, S. 2015, ApJ, 807, 108
Joinet, A., Kalemci, E., & Senziani, F. 2008, ApJ, 679, 655
Markoff, S., Falcke, H., & Fender, R. 2001, A&A, 372, L25
Markoff, S., Nowak, M. A., & Wilms, J. 2005, ApJ, 635, 1203
Miller, J. M., Parker, M. L., Fuerst, F., et al. 2013, ApJL, 775, L45
Miller-Jones, J. C. A., Jonker, P. G., Dhawan, V., et al. 2009, ApJL, 706, L230
Miyakawa, T., Yamaoka, K., Homan, J., et al. 2008, PASJ, 60, 637
Molina, M., Bassani, L., Malizia, A., et al. 2013, MNRAS, 433, 1687
Molina, M., Malizia, A., Bassani, L., et al. 2019, MNRAS, 484, 2735
Motta, S., Belloni, T., & Homan, J. 2009, MNRAS, 400, 1603
Narayan, R., McClintock, J. E., & Yi, I. 1996, ApJ, 457, 821
Newville, M., Stensitzki, T., Allen, D. B., & Ingargiola, A. 2014, LMFIT, Zenodo, doi:10.5281/zenodo.11813
Petrucci, P. O., Haardt, F., Maraschi, L., et al. 2001, ApJ, 556, 716
Plotkin, R. M., Miller-Jones, J. C. A., Gallo, E., et al. 2017, ApJ, 834, 104
Qiao, E., & Liu, B. F. 2013, ApJ, 764, 2
Rana, V., Loh, A., Corbel, S., et al. 2016, ApJ, 821, 103
Rani, P., Stalin, C. S., & Goswami, K. D. 2019, MNRAS, 484, 5113
Reid, M. J., McClintock, J. E., Narayan, R., et al. 2011, ApJ, 742, 83
Reid, M. J., McClintock, J. E., Steiner, J. F., et al. 2014, ApJ, 796, 2
Ricci, C., Ho, L. C., Fabian, A. C., et al. 2018, MNRAS, 480, 1819
Rodriguez, J., Corbel, S., & Tomsick, J. A. 2003, ApJ, 595, 1032
Steiner, J. F., McClintock, J. E., & Reid, M. J. 2012, ApJL, 745, L7
Svensson, R. 1984, MNRAS, 209, 175
Titarchuk, L., & Lyubarskij, Y. 1995, ApJ, 450, 876
Tortosa, A., Bianchi, S., Marinucci, A., et al. 2018, MNRAS, 473, 3104
Uttley, P., Gendreau, K., Markwardt, C., et al. 2018, ATel, 11423, 1
Verner, D. A., Ferland, G. J., Korista, K. T., & Yakovlev, D. G. 1996, ApJ, 465, 487
Walton, D. J., Mooley, K., King, A. L., et al. 2017, ApJ, 839, 110
Wilms, J., Allen, A., & McCray, R. 2000, ApJ, 542, 914
Wu, Q., & Gu, M. 2008, ApJ, 682, 212
Xie, F.-G., Niedźwiecki, A., Zdziarski, A. A., & Yuan, F. 2010, MNRAS, 403, 170
Xie, F.-G., Yang, Q.-X., & Ma, R. 2014, MNRAS, 442, L110
Yamaoka, K., Uzawa, M., Arai, M., Yamazaki, T., & Yoshida, A. 2005, ChJAS, 5, 273
Yan, Z., & Yu, W. 2017, MNRAS, 470, 4298
Yang, Q.-X., Xie, F.-G., Yuan, F., et al. 2015, MNRAS, 447, 1692
Younes, G., Porquet, D., Sabra, B., & Reeves, J. N. 2011, A&A, 530, A149
Yu, X.-F., Gu, W.-M., Liu, T., Ma, R.-Y., & Lu, J.-F. 2015, ApJ, 801, 47
Yuan, F., & Narayan, R. 2014, ARA&A, 52, 529
Yuan, F., Taam, R. E., Misra, R., Wu, X.-B., & Xue, Y. 2007, ApJ, 658, 282
Yuan, F., & Zdziarski, A. A. 2004, MNRAS, 354, 953
Zdziarski, A. A. 2016, A&A, 586, A18
Zdziarski, A. A., Johnson, W. N., & Magdziarz, P. 1996, MNRAS, 283, 193
Zdziarski, A. A., Lubiński, P., Gilfanov, M., & Revnivtsev, M. 2003, MNRAS, 342, 355